European Polymer Journal 49 (2013) 1897–1906

Contents lists available at SciVerse ScienceDirect

European Polymer Journal

journal homepage: www.elsevier.com/locate/europolj

Feature Article

# Nanomechanical mapping of soft matter by bimodal force microscopy

Ricardo Garcia [a,*], Roger Proksch [b]

[a] Instituto de Ciencia de Materiales de Madrid (CSIC), 28049 Madrid, Spain
[b] Asylum Research, an Oxford Instruments Company, Santa Barbara, CA 93117, USA

ARTICLE INFO

*Article history:*
Received 19 March 2013
Accepted 27 March 2013
Available online 13 April 2013

*Keywords:*
Force microscopy
Nanomechanics
Bimodal AFM
Soft matter

ABSTRACT

Bimodal force microscopy is a dynamic force-based method with the capability of mapping simultaneously the topography and the nanomechanical properties of soft-matter surfaces and interfaces. The operating principle involves the excitation and detection of two cantilever eigenmodes. The method enables the simultaneous measurement of several material properties. A distinctive feature of bimodal force microscopy is the capability to obtain quantitative information with a minimum amount of data points. Furthermore, under some conditions the method facilitates the separation of the topography data from other mechanical and/or electromagnetic interactions carried by the cantilever response. Here we provide a succinct review of the principles and some applications of the method to map with nanoscale spatial resolution mechanical properties of polymers and biomolecules in air and liquid.



**Contents**



## 1. Introduction

The emergence of hybrid devices and materials made up of nanostructures of different mechanical, chemical, electric and/or magnetic properties requires the development of non-invasive, high resolution and fast characterization methods that combine high spatial resolution with compositional contrast. Ideally, those materials should be observed in their native environment and state. The atomic force microscope (AFM) [1] has significantly contributed to our current understanding of soft-matter interfaces [2–5]. Conversely, the evolution of the atomic force

* Corresponding author.
*E-mail addresses:* r.garcia@csic.es (R. Garcia), roger@AsylumResearch.com (R. Proksch).

0014-3057/$ - see front matter © 2013 Elsevier Ltd. All rights reserved.
http://dx.doi.org/10.1016/j.eurpolymj.2013.03.037

microscope (AFM) is being shaped by the need to provide a full characterization of complex interfaces [6]. Images of heterogeneous surfaces with high spatial resolution (sub-5 nm range) in combination with compositional contrast have been provided by dynamic AFM methods such as phase imaging [4,7–17]. This method enables to identify and measure energy dissipation processes at the nanoscale [9–13]. In general it is not straightforward to transform those images into quantitative information about other nanomechanical properties albeit some notable exceptions exist [7,9,14–16].

Force microscopy has provided a nearly continuous progress in high resolution imaging-nano, molecular or atomic-of materials by experiencing multiple transformations. This has led to the development a large variety of dynamic force-based methods [6,18–24]. The common thread in those methods is the detection of forces and the use a mechanical cantilever-tip system as the transducer of the forces.

Bimodal force microscopy is an AFM method that uses several eigenmode frequencies for excitation and detection [19,25,26]. The different resonances act as signal channels that allow accessing and separating material properties such as topography, dissipation, Young modulus, viscosity and short and long-range interactions.

To facilitate the understanding of bimodal AFM it is convenient to distinguish between some of the major frequency components carried out by the cantilever-tip response, eigenmodes and harmonics. The cantilever-tip ensemble, cantilever or probe for short, is a mechanical system which has a number of discrete oscillations $\omega_j$ with $j = 1, 2, \ldots$ that are determined the boundary conditions. Those oscillations are variously termed 'eigenmodes', 'normal modes' or 'resonances'. When the normal modes are contained in a plane orthogonal to the main plane of the cantilever they are called flexural modes. A higher harmonic, on the other hand is a component of the oscillation that vibrates with a frequency that is equal to an integer multiple of the excitation frequency ($\omega_n = n\omega$). In general, higher harmonic and resonant frequencies do not coincide. Subharmonics are components with a frequency that is a submultiple of the excitation frequency. The harmonics are introduced in the probe motion by the nonlinearities in the interaction force. A more complete description of eigenmodes and harmonics in the context of AFM can be found elsewhere [6,27–29]. Fig. 1a shows the first two flexural mode shapes of a rectangular cantilever that is clamped at one end and free to oscillate at the other.

## 2. Bimodal AFM

### 2.1. Operating principles

The method uses two driving forces to excite the vibration of the cantilever. The excitation frequencies of the driving forces are tuned to match two of the eigenmodes of the cantilever, usually the first and the second flexural modes of the cantilever,

$$F_{exc} = F_1 \cos \omega_1 t + F_2 \cos \omega_2 t \quad (1)$$

then the cantilever response can be expressed

$$z = z_0 + A_1 \cos(\omega_1 t - \phi_1) + A_2 \cos(\omega_2 t - \phi_2 t) + \xi \quad (2)$$

where $F_i$, $\omega_i = 2\pi f_i$, $\phi_i$, $A_i$ are, respectively, the excitation force, angular frequency, phase shift and amplitude of the eigenmode $i$. The last term $\xi$ represents the deflection components at frequencies different of the excited ones. Those components are usually neglected.

A scheme of the addition of the first two modes and the resulting excitation signal is shown in Fig. 1b and c. In the most common experimental set-up, an output signal of the first mode (either the amplitude or the frequency shift) is used to image the topography of the surface while the output signals of the second mode (amplitude, frequency shift and/or phase shift) are used to measure changes in different mechanical [30–38], magnetic [39,40] or electrical properties [41–44] of the surface. This method is compatible with both dynamic AFM modes, amplitude (AM) and frequency modulation (FM) modes [45]. It can be operated in air [25,26], liquid [31] or ultrahigh vacuum [46,47].

### 2.2. Bimodal AFM configurations

The variety of observables to record the tip-surface force and to operate the feedback has produced several bimodal AFM configuration modes. This makes bimodal AFM very flexible and, at the same time, the subtleties of the different configurations might be hard to follow.

Computer simulations laid the foundations [19] for the experimental implementation of bimodal AFM. The first bimodal AFM prototypes had the feedback controlling the amplitude of the 1st resonance while the parameters of the second resonance were free to change (open loop) [25,26]. This configuration is called amplitude modulation (AM). By operating the feedback in the frequency shift of the first mode instead of the amplitude a new bimodal configuration is in place [48,56], this bimodal AFM configuration is termed (FM). A combination of the feedbacks in the amplitude of the first resonance and the frequency shift of the second gives rise to the configuration known as AM–FM [34]. Table 1 shows a classification of some of the current bimodal AFM configurations.

Kawai and co-workers have proposed a bimodal AFM operation scheme that involves the excitation of a flexural mode and a torsional mode [48]. Solares and Chawla have demonstrated that the cantilever excitation/detection scheme could be extended to three normal frequencies. They called this approach trimodal AFM [49,50].

### 2.3. The physics of bimodal AFM

The understanding of bimodal AFM contrast is still under development [48,51–53]. This is partly due to the novelty of the method. The intrinsic flexibility of bimodal AFM operation to select the observable for material contrast complicates the development of a coherent framework that encompasses all the bimodal AFM variations [34]. Nonetheless, there are some established principles that explain the properties of bimodal AFM in terms of the force sensitivity, the compositional contrast or the ability to separate the various forces acting on the cantilever.

Three main factors singularize bimodal AFM operation [51]: the coupling between excited modes induced by the nonlinear tip-surface force, doubling of the number of

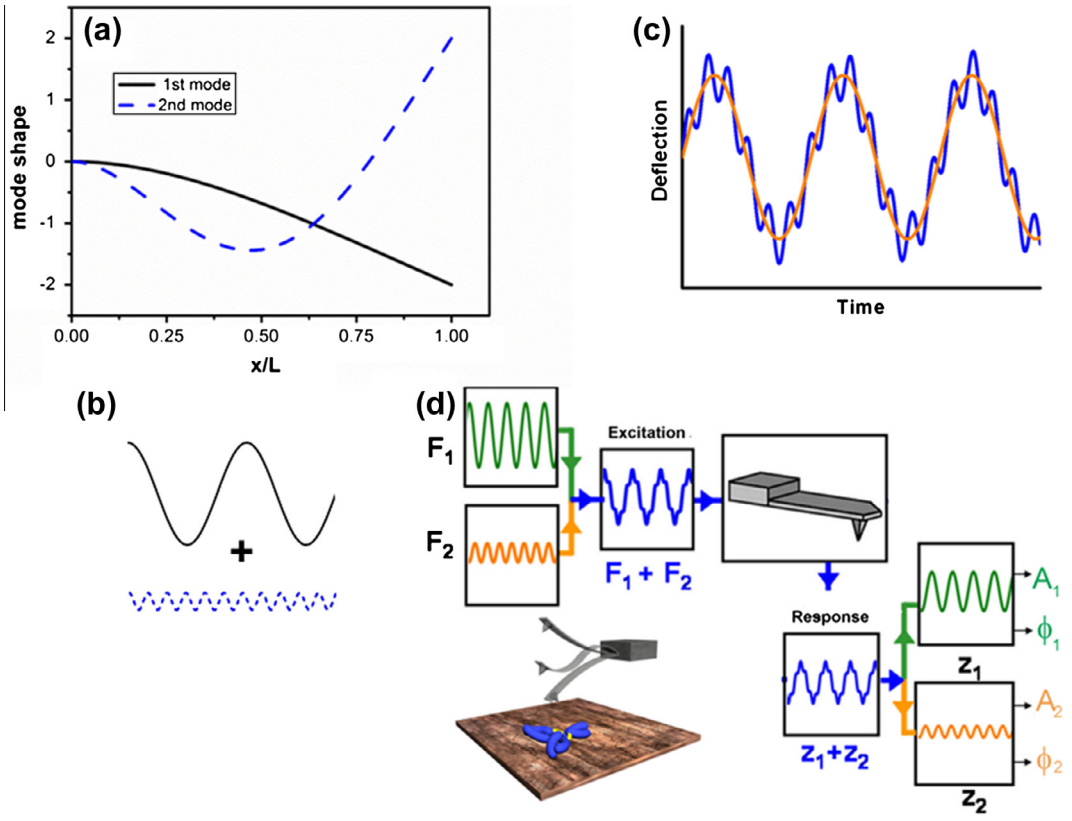


**Fig. 1.** (a) Mode shapes of the first two flexural modes of tipless rectangular cantilever beam. (b) Scheme of the combination of two frequencies in bimodal AFM and resulting tip excitation (c). (d) Diagram of bimodal AFM excitation and detection in the AM configuration.

**Table 1**
Bimodal AFM configurations.

| Mode name | Feedback mode 1 | Feedback mode 2 | Observables | Quantitative observables[a] | Material property |
|---|---|---|---|---|---|
| Bimodal AM | AM | Open | $A_1$, $A_2$, $\phi_1$, $\phi_2$ | $\phi_1$ | Dissipation |
| Bimodal AM–FM | AM | FM | $A_1$, $A_2$, $\phi_1$, $\phi_2$, $\Delta f_2$ | $\Delta f_2$ | Dissipation, stiffness, Young modulus, |
| Bimodal FM | FM | Open | $A_1$, $A_2$, $\phi_1$, $\phi_2$, $\Delta f_2$ | $\phi_1$, $A_2$, $\phi_2$ | Dissipation, stiffness, Young modulus |

[a] Observables that have an analytical relationship with a nanoscale property.

observables to record information on material properties and the lack of feedback restrictions for the additional excited mode. The eigenmodes of a cantilever have different force constants, quality factors and resonant frequencies [6,27], consequently they do not offer the same sensitivity to detect material properties.

Let's start with a discussion about the origin of bimodal AFM contrast in an heterogeneous surface. In general the tip-surface force can be separated into conservative and non-conservative (dissipative) components [54],

$$F_{ts} = F_{con} + F_{dis} \tag{3}$$

In amplitude modulation AFM, the use of time-averaged models, usually expressed in terms of the virial and energy conservation [45,55], enables the deduction of some analytical or semianalytical expressions connecting the observables and the mean values of forces and energies [51,52], for example, the phase shift of an excited mode $\phi_i$ is expressed as,

$$\phi_i = \phi_i[V_{ts}(i), E_{dis}(i)] \tag{4}$$

where $V_{ts}(i)$ and $E_{dis}(i)$ are, respectively, the virial of the force and the energy dissipated on the trajectory of mode $i$. In amplitude modulation AFM, the amplitude of the first mode remains fixed during imaging $A_1 = A_{sp}$ and as a consequence

$$\phi_1(x,y) = \phi_1[E_{dis}(1)](x,y) \tag{5}$$

If the experiment is performed under the absence of non-conservative forces or when non-conservative forces are negligible with respect to the conservative forces.

$$\phi_1 = \phi_1(x,y) = fixed \tag{6}$$

Consequently no changes in the phase shift will be observed during imaging. However, in the bimodal AFM con-

figuration where the second mode is free (either AM or FM in Table 1) the above condition does not apply to the second mode,

$$\phi_2 = \phi_2[V_{ts}(2)](x,y) \tag{7}$$

Bimodal AFM operation facilitates to combine robust and stable imaging conditions with quantitative and compositional measurements by using different amplitudes for the topographic imaging (usually $A_1$) and for the additional mode (quantitative). Optimum working operations have been set to ratios of $A_1/A_2 \leqslant 10$ with $A_2 < 1$ nm. The small value of $A_2$ with respect to the scale where the interaction force changes might allow to develop an analytical relationship between the gradient of the interaction force and phase shift of the second mode [56],

$$F'_{ts,peak}(z_c) \approx C\frac{k_2 A_{02}}{Q_2 A_2(z_c)}\cos\phi_2(z_c) \tag{8}$$

where $Q_2$ and $k_2$ are respectively the quality factor and force constant of the second mode. Then by using Hertz contact mechanics a relationship between the $\phi_2$ and the local Young modulus of the tip-surface interface $E_{eff}(x, y)$ is obtained,

$$F'_{ts,peak}(z_c) \approx 2E_{eff}\sqrt{R(a_0 - d_{\min})} = 2E_{eff}r_c \tag{9}$$

$$E_{eff} = \frac{F'_{ts,peak}(z_c)}{2r_c} \tag{10}$$

where

$$\frac{1}{E_{eff}} = \frac{1-\nu_t^2}{E_t} + \frac{1-\nu_s^2}{E_s} \tag{11}$$

whenever, the Young modulus of the tip ($E_t \sim 160$ GPa) is much larger than the Young modulus of the sample for silicon $E_s$, the effective Young modulus of the interface can be approximated for that of the sample $E_{eff} \approx E_s$. This the common situation while imaging soft matter ($\nu_s \sim 0.4$).

## 3. Nanomechanical mapping of soft-matter

The experimental bimodal AFM configuration used here is the AM–FM (Table 1). In this configuration the topographic feedback is performed in the amplitude modulation mode and it is confined to the first resonant mode which means much greater stability. For example, if the phase-locked loop (PLL) or automatic gain control (AGC) keeping the response amplitude constant feedback control loops operating on the second mode become unstable and oscillate, it has little or no effect on the ability of the first mode to track the surface topography. The second excited mode is used to measure the Young modulus by following frequency shifts. In particular, the frequency shift of a cantilever in frequency modulation mode is given by [57]

$$\Delta f_2 = -f_{0,2}\frac{\langle F_{ts}z\rangle}{k_2 A_2^2} \tag{12}$$

where $f_{0,2}$ is the second resonant frequency measured at a "free" or reference position, $\Delta f_2$ is the shift of the second resonant mode as the tip interacts with the surface, $k_2$ is the stiffness of the second mode and $A_2$ is the amplitude of the second mode as it interacts with the surface. As with the expression for the loss tangent [58] since it involves a ratio of amplitudes, it does not directly involve the optical lever sensitivity. Thus, we can relate the measured frequency shift to a tip-sample stiffness $k_{ts}$

$$k_{ts} \approx \frac{2k_2\Delta f_2}{f_{0,2}} \tag{13}$$

Since the frequency shift of second mode depends on the interaction stiffness $k_{ts}$, the material modulus can be measured and mapped by applying a particular mechanical model. One of the most simple models is a Hertz indenter in the shape of a punch. In this case, the elasticity of the sample is related to the tip-sample stiffness by the relation

$$k_{ts} = 2E_{eff}r_c \tag{14}$$

by combining Eqs. (13) and (14) the following expression is deduced for the Young modulus

$$E_{eff} = \frac{\Delta f_2}{f_{0,2}}\frac{k_2}{r_c} \tag{15}$$

Thus if the contact area can be approximated by $(\pi r_c^2)$ and the spring constant are known, the sample modulus can be calculated. Of course, other tip shapes could be used in the model. Calibration of the tip shape is a well-known problem, beyond the scope of this paper. However, it is possible to use a calibration sample that circumvents this process. As a first step, we have used a traceable ultra high molecular weight high density polyethelene (UHMWPE) [59] reference sample to first calibrate the response of the cantilever. Eq. (15) can be rewritten as

$$E_{eff} = C_2\Delta f_2 \tag{16}$$

where $C_2$ is a constant, measured over the UHMWPE reference that relates the frequency shift to the elastic modulus. This can then be applied to unknown samples. The above expressions can be generalized for cases where the second excited mode is a higher cantilever mode different from the second mode, by replacing the sub-index 2 by the index $i$ of the higher excited mode.

Fig. 2 shows two bimodal AFM images of two different polymer surfaces. A bimodal AFM image of a three component blend of polypropylene (PP), polyethylene (PE), polystyrene (PS) in the relative proportion of 60% PE, 20%PS and 20% PP is shown Fig. 2a. Fig. 2b shows the bimodal AFM image of a high density polyethelene surface. The bimodal AFM image does not show any contrast because the surface is homogeneous. The histogram in Fig. 2c shows the frequency shift of the third mode of the different polymers. The correlation of the effective Young modulus and the frequency shift is shown in Fig. 2d.

The above method can also be performed at higher speeds using small cantilevers. In this case the response bandwidth of the $i$th resonant mode of a cantilever is

$$BW_i = \pi f_{0,i}/Q_i \tag{17}$$

where $f_{0,i}$ is the resonant frequency of the $i$th mode and $Q_i$ is the quality factor. To increase the resonant frequency without changing the spring constant requires the use on

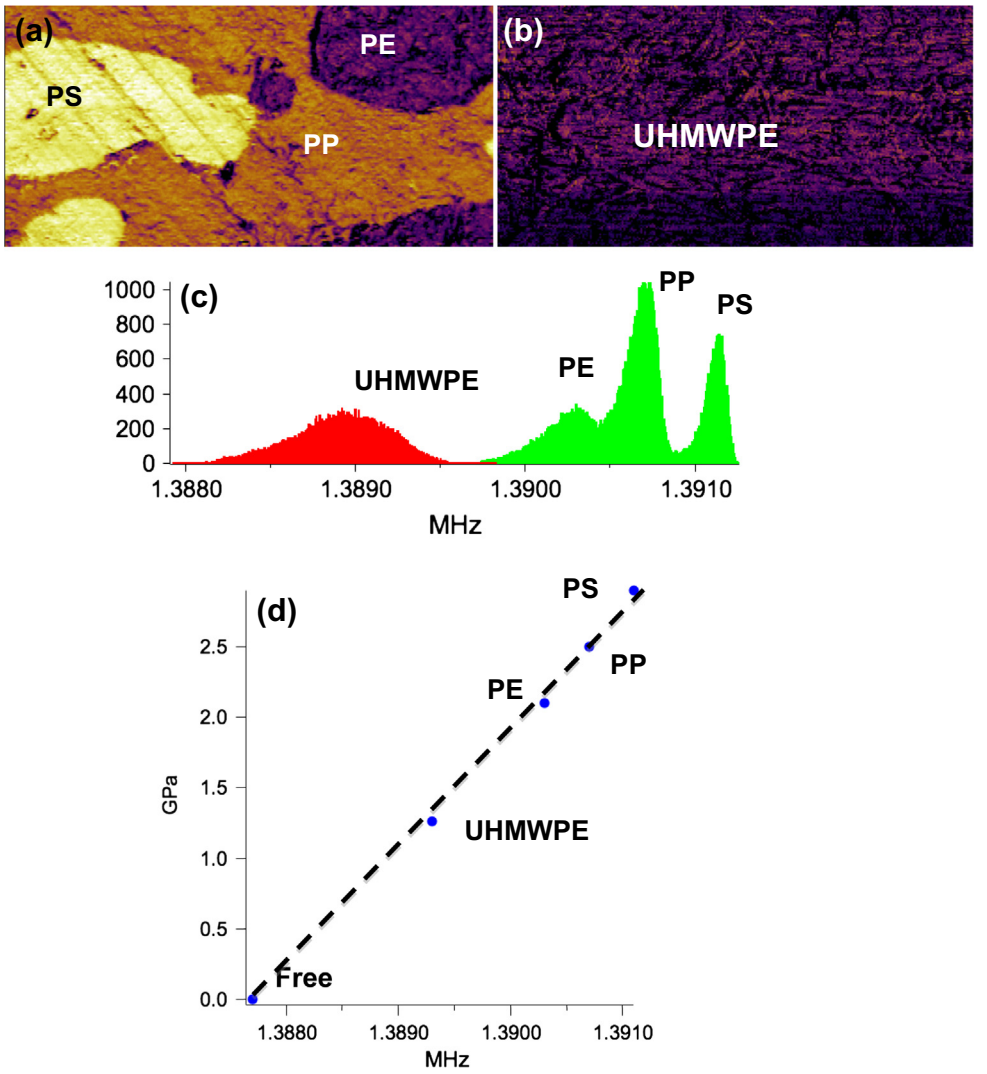


**Fig. 2.** Bimodal AFM images of polymer surfaces. The images are taken in the bimodal AM–FM configuration. (a) Bimodal AFM images of a polypropylene (PP), polyethylene (PE), polystyrene (PS) "Ternary" blend and (b) ultra-high molecular weight Polyethylene (UHMWPE) surface acquired to provide a reference value for the Young modulus. (c) Histogram of the third mode frequency shifts measured over the images (a and b). (d) Shows the expected moduli plotted versus the third mode frequency, showing a roughly linear relation. The higher order resonances were measured while a feedback loop on the tip-sample separation was operated to keep the first mode amplitude constant. An AC160 cantilever from Olympus has been used. Sample courtesy of D. Yablon and A. Tsou, Corporate Strategic Research, ExxonMobil, New Jersey.

small cantilevers [60]. In contrast to conventional amplitude modulation AFM imaging, the second resonant mode must still be accessible to the photodetector, requiring that the frequency is below its maximum bandwidth [61]. An example is shown in Fig. 3 where an ethylene propylene diene monomer EPDM rubber/Epoxy cryo-microtomed boundary is measured at a 2 Hz and 20 Hz line scan rates. The main features observed in both images do not significantly depend on the scan rates used for imaging. The Young modulus of the softer region (~3 GPa) shows a small displacement to a higher value (~3.5 GPa). The above images were acquired with a cantilever with resonant frequencies $f_{0,1} \approx 1.3MHz, f_{0,2} = 5.3MHz$. Note that the frequency shifts of the second mode in both cases were on the order of 20 kHz, a small perturbation with respect to the mode frequency.

## 4. Mapping protein flexibility with sub-2 nm resolution

Flexibility plays a central role in protein–protein binding. Current methods for the determination of protein flexibility give results in a time scale of picoseconds [62] that might not provide relevant information to the conditions where proteins have conformational changes in physiological conditions (micro- to milliseconds). Martinez-Martin et al. have implemented the frequency modulation configuration to bimodal AFM to measure the local variations of the elastic modulus of a single protein in liquid simultaneous with topography [56].

Fig. 4 shows a bimodal AFM image of the topography and flexibility of a single IgM antibody. The flexibility map is expressed as for the above cases in terms of the local variations of the Young modulus $E_{eff}(x,y)$. However, in

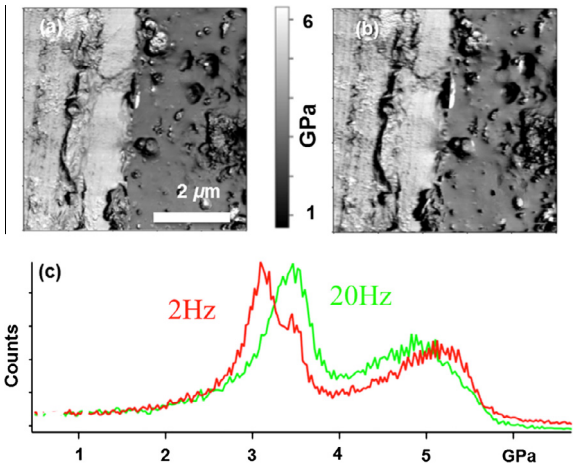


**Fig. 3.** Fast bimodal AM–FM elasticity images of a cryomicrotomed epoxy/EPDM (ethylene propylene diene monomer) rubber bond imaged at 2 Hz (a) bonded sandwich imaged at 2 Hz (a) and at 20 Hz (b) line scan rates. (c) Elasticity histogram at the different imaging frequencies. Images taken with an AC55 cantilever (Olympus corporation, Japan). The scan size in both images is 5 μm.

this case the Young modulus is determined by recording $A_2(x, y)$ and $\phi_2$(x, y) and using Eqs. (8)–(10) to determine $E_{eff}$ from the observables. The flexibility map shows a maximum of 19.0 ± 0.1 MPa and a minimum value of 8.2 ± 0.1 MPa. The uppermost part of the protein complex is stiffer section as a consequence of the presence of *j*-chain and the five Fc elements of each arm. Another stiffer is the region of the Fab arms that is linked to the Fc. On the other hand, low elastic modulus values are found in the last domain of the Fab arms. The above findings are consistent with the orientation flexibility of the antibody complex when its binds a cell surface antigen. Remarkably, the softer regions are found at the end of the Fab arms. Those regions are closer to the mica surface which has a Young modulus about three orders of magnitude higher than the protein. This illustrates that the measurements are not affected by the elastic modulus of the mica surface. It is remarkable to observe that values obtained here are comparable to the values reported for packed arrays of proteins (5–50 MPa) [23,63].

A key factor to obtain the above map was the application of very small maximum or peak forces (~50 pN). The noninvasive character of the measurements was verified by comparing the nominal height of the protein complex (~8 nm) and the height measured by the AFM (~6–7 nm). The difference between the observed and the nominal heights can be explained by the deformation experienced by the subunits of the protein complex due to its adsorption on the mica surface.

## 5. Imaging superparamagnetic ferritin with a lateral resolution of 5 nm

Bimodal AFM could be used to separate short and long-range interactions by tuning each excited mode to be more sensitive to a given interaction. Lin et al. have demonstrated that bimodal AFM could image magnetic structures in a single pass [39], in this way improving data acquisition times with respect to standard magnetic force microscopy (MFM) method (lift mode) that involves two passes, one for the topography and the other for the magnetic interaction [64].

The resolution and sensitivity of bimodal magnetic force microscopy is illustrated by its ability to image magnetic nanoparticles with a lateral resolution in the sub-10 nm range. Dietz et al. [40] have imaged magnetic polarized single ferritin proteins in air and liquid with a spatial resolution of 5 nm. Ferritin is a cage-shaped biomolecule that accommodates an iron oxyhydroxide nanoparticle. This protein is formed by a polypeptide hollow shell (apoferritin) that encapsulates a superparamagnetic iron-based core that can reach a maximum diameter of 7 nm.

Fig. 5 shows two images obtained in buffer (pH = 3) of a mixture of ferritin and apoferritin molecules. The topography shows a random distribution of nanoparticles. On the other hand, the phase shift image $\phi_2$ shows two different morphologies, ring-like and flat disk structures (Fig. 5b). The ring-like structure is associated with ferritin while the flat-disk is associated with apoferritin. The phase shift cross-section of the proteins (Fig. 5c) shows that apoferritin is characterized by a rectangular shape while ferritin is characterized by the presence of two peaks and a dip in between. The ring-like shape of ferritin in liquid is explained by the interplay between magnetic and mechanical

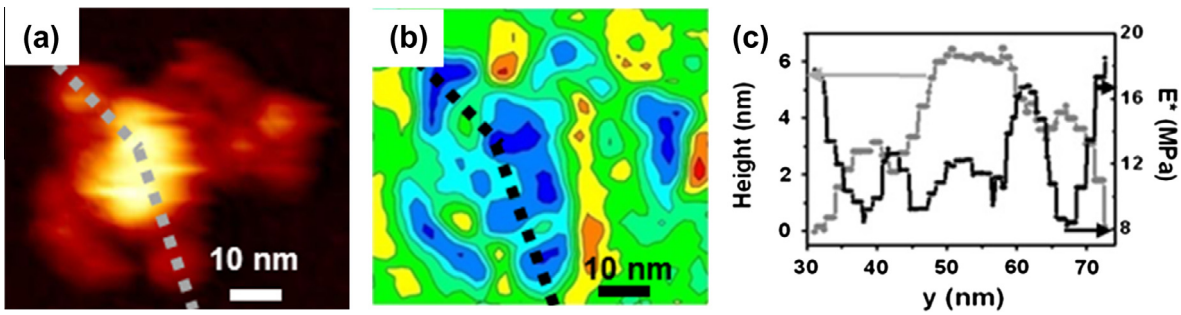


**Fig. 4.** Topography and flexibility map of a single IgM antibody. (a) Bimodal FM–AFM image taken at $\Delta f$ = 40 Hz (peak force of 40 pN), $A_1$ = 4.5 nm and $A_{02}$ = 0.5 nm. (b) Flexibility map obtained simultaneously with the topography image by recording the bimodal parameters ($A_2$, $\phi_2$). (c) Topography (grey) and flexibility (black) profiles along the lines marked, respectively, in a and b. Data obtained from Martinez-Martin et al. [56].

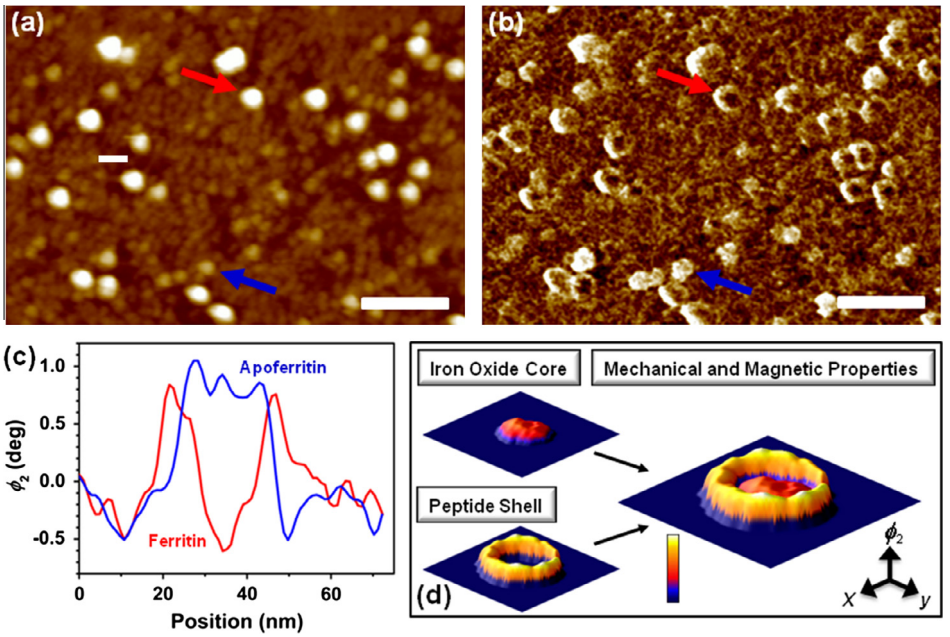


**Fig. 5.** Topography and bimodal phase shift images in buffer (pH = 3) of a sample containing a mixture of ferritin and apoferritin molecules. (a) Topography ($A_{0,1}$ = 7 nm, $A_{sp}$ = 6 nm, $A_{0,2}$ = 1.1 nm). (b) Bimodal phase shift image of (a). The phase image shows two different structures are observed, ring-like and full nanoparticles. (c) Phase shift cross-section of the nanoparticles marked in (a) and (b). (d) Separation of the iron oxide core and apoferritin shell of the nanoparticles. The phase shift of the iron oxide core has been obtained by subtracting the phase shift given $A_1$ = 6 nm by the mechanical forces of the protein shell and the one obtained in a ferritin nanoparticle (ring-like structure). Scale bar is 100 nm. Data obtained from Dietz et al. [40].

interactions and the enhancement of magnetostatic interactions in the bimodal phase shift [40]. Dynamic AFM imaging in liquid is usually performed under a net repulsive force. When the tip is over an apoferritin molecule, the short-range mechanical forces give rise to the topography and the bimodal phase shift images. When the tip is over a ferritin molecule, the short-range mechanical forces control the amplitude decrease as in the apoferritin case and the topography is recorded. However, the bimodal phase shift is sensitive to the presence of both short-range mechanical (repulsive) and long-range magnetic (attractive) forces. Those forces drive the bimodal phase shift in opposite directions. When the tip is on top of the ferritin the magnetic interaction is maximized and a depression in the phase shift-cross section is observed. The reconstructed image of the ferritin with its mechanical shell and magnetic core is shown in Fig. 5d.

The above images show an improvement of the resolution to image and detect magnetic interactions (nanoparticles) by a factor 2 with respect to conventional MFM. The data also show that imaging magnetic interactions-in air or liquid – with a spatial resolution of 1 nm could be feasible.

## 6. Three-dimensional images of protein–liquid interfaces

Molecular resolution images of solid–liquid interfaces represents one of the frontiers in high resolution imaging. The flexibility and the potential of bimodal AFM to bring information about novel properties is exemplified by the experiments performed to study the spatial and time-evolution of water layers adsorbed on solid surfaces [65]. The technique enables the three-dimensional imaging and mapping of the hydration layers and forces on mica and protein GroEL surfaces with 10 piconewton, 2 Å and 40 s (whole volume) resolutions.

The approach developed by Herruzo et al. [65] measures the static and dynamic three-dimensional force field of solid–water interfaces by detecting the changes in the AFM observables with the *xyz* position of the probe. Those changes are associated with variations in the forces acting between the tip and the water interface which, in turns, are related to changes of the solid–liquid interface such as the local stiffness, the density of the water or the incoming of an external nanoparticle.

In bimodal three-dimensional AFM the tip scans the *xy* plane parallel to the sample surface as it is also displaced in the perpendicular *z* axis (Fig. 6a). The feedback mechanism acts on the amplitude $A_1$. It establishes a mean tip-surface distance $z_c$ for imaging like in regular amplitude modulation AFM. Then the tip-surface separation is modulated as the tip scans laterally as $z_c \pm \Delta z_m$ to generate the 3D maps of the solid–liquid interface. During the modulation, the observables will change following the changes of the interface. In the above experiments the frequency of the $\Delta z$ modulation was 195 Hz which enables a 5 ms time resolution.

Fig. 6c shows the full three-dimensional data obtained on a mica–water interface. The 3D maps could be assembled by either presenting the data from the *xz* or the *xy* planes. Fig. 6b shows a 3D-AFM image of the mica-water interface formed by gathering *xz* data. In the proximity of

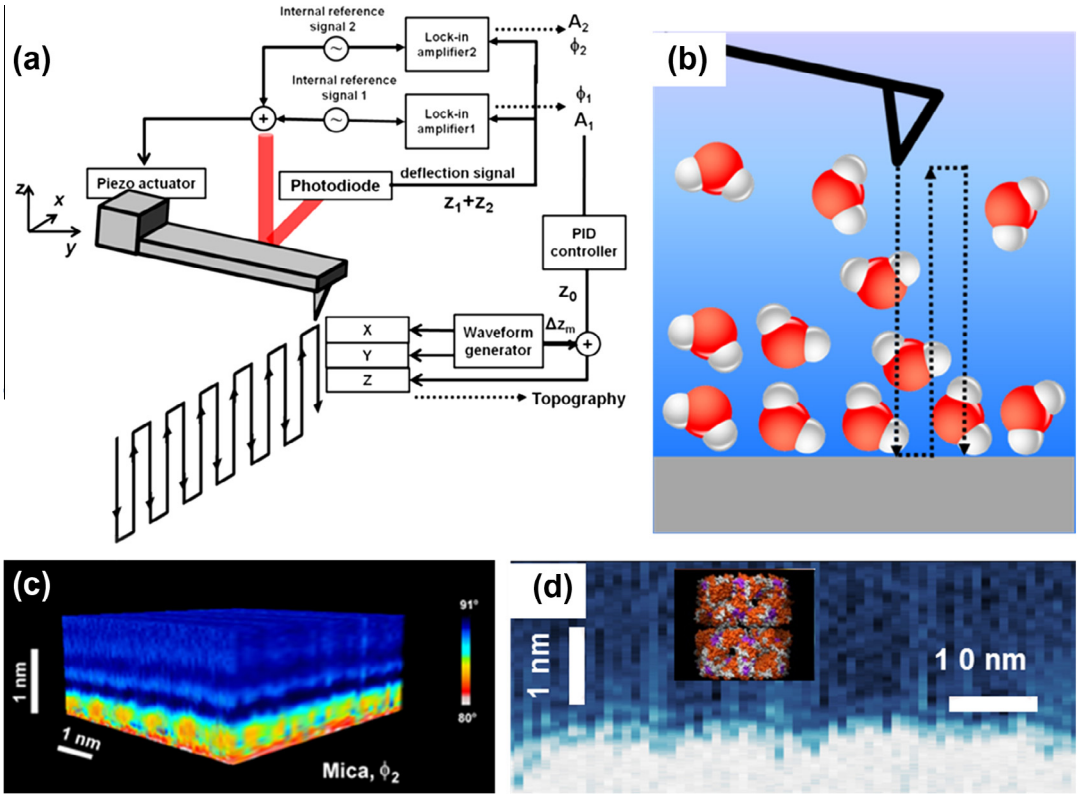


**Fig. 6.** (a) Block diagram of bimodal excitation and 3D scheme for the tip motion. In bimodal 3D-AFM the microcantilever is driven simultaneously at the frequencies of the first two flexural modes. Additionally a modulation is applied to the *z*-piezo ($\Delta z_m$) at the same time that the tip is displaced over a *xy* plane of the interface (rectangular waveform). (b) Scheme of the operation of the AFM in a solid–water interface. (c) 3D image of a mica–water volume. The color scale shows variations of $\phi_2$. The side view shows two hydration layers on mica. The contrast observed in $\phi_2$ enables resolving atomic-resolution features on the mica surface. (d) *xz* cross-section of the protein–liquid interface ($\phi_1$ ($x$, $y_0$, $z$)). The hydration layers follow the contours of four GroEL molecules. The edges separating the proteins are resolved in the image. The dashed line marks the contours of the proteins. The inset shows a side view of the GroEL structure as obtained by diffraction methods [66] (protein data bank 1KPO)[65].

the mica, the phase shift shows some distinct oscillations. Those oscillations are also seen in other observables. The observed periodicity is close to the nominal size of a water molecule which suggests the presence of hydration layers. The 3D-AFM image also shows the atomic structure of the mica. The bimodal 3D-AFM mode has also been applied to study the formation of hydration layers on protein surfaces. GroEL proteins were chosen because they have a well-defined ring structure [66] that tends to form organized two dimensional arrays when deposited on a mica surface [67]. GroEL has 14 subunits arranged in two back-to-back rings (cis and trans) made out of seven subunits each. The ring is 14 nm in diameter, 15 nm in height. The internal channel is about 4.5 nm in diameter. The *xz* cross-sections show the alternation of light and dark stripes that are modulated by the contour structure of the GroEL (~14 nm) (Fig. 6d). A pattern of light–dark stripes indicate the presence of interfacial hydration layers on top of the proteins. The average width of the light–dark sequence is 0.31 nm, a value close to the diameter of a single water molecule (~0.28 nm). The change in amplitude between the light–dark regions for the 1st and 2nd hydration layers is 140 pm and 10 pm respectively. Those values illustrate the compatibility of bimodal AFM with very high vertical sensitivity.

## 7. Summary and outlook

Bimodal atomic force microscopy is an emerging dynamic AFM method that involves the simultaneous excitation and detection of two cantilever modes. It is characterized by rapid, gentle and reproducible imaging at extreme high resolution. This advanced force microscopy method has the potential to materialize some long-lasting goals of force microscopy such as the simultaneous and fast quantitative imaging of topography and material properties in air and liquid. Bimodal AFM has a variety of configurations depending on whether the feedback is modulated in amplitude, frequency or both. Remarkably some of the bimodal AFM configurations enable the deduction of direct and relatively simply analytical relationships between the observables and the material properties.

We have described several applications involving polymers and biomolecules in both air and liquid environments that underlined some of the most innovative features brought by this force microscopy method. The different regions of a ternary polymer blend have been separated and their respective Young modulus measured. Quantitative nanomechanical mapping is compatible with fast scan rates. This has been illustrated by measuring the elastic modulus variations of a polymer surface at 2 and 20 Hz

scan rates, yielding values of the Young modulus that are independent of the scan rate.

The combination of quantitative and high resolution imaging in liquid has been illustrated by imaging the flexibility of an isolated antibody in water. Young modulus variations between 8 and 19 MPa have been measured with a spatial resolution of 2 nm. The above experiment also illustrates the compatibility of bimodal operation with imaging at sub-50 pN peak forces. Superparamagnetic proteins have been imaged in liquid. The magnetic contribution from the iron oxide core has been imaged with a lateral resolution of 5 nm. Those experiments illustrate the ability of bimodal AFM to separate long-range magnetic from short-range mechanical interactions.

Quantitative and high resolution imaging by bimodal AFM is not restricted to solid surfaces. The last application described in this report shows the three-dimensional imaging of mica and protein–water interfaces with atomic spatial resolution and a 10 pN force sensitivity.

## Acknowledgements

R.G. thanks the financial support from the Ministerio de Economía y Competitividad (Consolider Force-For-Future, CSD2010-00024, MAT2009-08650) and the Comunidad de Madrid S2009/MAT-1467.

## References

[1] Binnig G, Quate CF, Gerber C. Atomic force microscope. Phys Rev Lett 1986;56:930.
[2] Vancso GJ, Schön P, Duvigneau J. What's new in AFM of polymers ?. An update. Microsc Anal 2009;23:5–11.
[3] Hobbs JK, Farrance OE, Kailas L. How atomic force microscopy has contributed to our understanding of polymer crystallization. Polymer 2009;50:4281–92.
[4] Garcia R, Magerle R, Perez R. Nanoscale compositional mapping with gentle forces. Nat Mater 2007;6:405.
[5] Gan Y. Atomic and subnanometer resolution in ambient conditions by atomic force microscopy. Surf Sci Rep 2009;64:99–121.
[6] Garcia R, Herruzo ET. The emergence of multifrequency force microscopy. Nat Nanotechnol 2012;7:217–26.
[7] Voitchovsky K et al. Direct mapping of the solid–liquid adhesion with subnanometre resolution. Nat Nanotechnol 2010;5:401–5.
[8] Spitzner EC, Riesch C, Magerle R. Subsurface imaging of soft polymeric materials with nanoscale resolution. ACS Nano 2011;5:315–20.
[9] Garcia R, Gomez CJ, Martinez NF, Patil S, Dietz C, Magerle R. Identification of nanoscale dissipation processes by dynamic atomic force microscopy. Phys Rev Lett 2006;97:016103.
[10] Martinez NF, Garcia R. Measuring phase shifts and energy dissipation with amplitude modulation atomic force microscopy. Nanotechnology 2006;17:S167–72.
[11] Santos S, Thomson NH. Energy dissipation in a dynamic nanoscale contact. Appl Phys Lett 2011;98:013101.
[12] Santos S et al. How localized are energy dissipation processes in nanoscale interactions? Nanotechnology 2011;22:345401.
[13] Gomez CJ, Garcia R. Determination and simulation of nanoscale energy dissipation processes in amplitude modulation AFM. Ultramicroscopy 2010;110:626–33.
[14] Melcher J, Xu X, Raman A, Carrasco-Pulido C, Gomez-Herrero J, de Pablo PJ, et al. Origins of phase contrast in the atomic force microscope in liquids. Proc Natl Acad Sci USA 2009;106:13655–60.
[15] Payam AF, Ramos JR, Garcia R. Molecular and nanoscale compositional contrast of soft matter in liquid: interplay between elastic and dissipative interactions. ACS Nano 2012:64663–70.
[16] Liu YH, Wang D, Nakajima K, Zhang W, Hirata A, Nishi T, et al. Characterization of nanoscale mechanical heterogeneity in a metallic glass by dynamic force microscopy. Phys Rev Lett 2011;106:125504.
[17] Kuna J, Voitchovsky Singh C, Jiang H, Mwenifumbo S, et al. The effect of nanometer-scale structure on interfacial energy. Nat Mater 2009;8:837–42.
[18] Barth C, Foster AS, Henry CR, Shluger AL. Recent trends in surface characterization and chemistry with high-resolution scanning force methods. Adv Mater 2011;23:477–501.
[19] Rodriguez TR, Garcia R. Compositional mapping of surfaces in atomic force microscopy by excitation of the second normal mode of the cantilever. Appl Phys Lett 2004;84:449.
[20] Killgore JP, Kelly JY, Stafford C, Fasolka M, Hurley DC, Fasolka MJ. Quantitative subsurface contact resonance force microscopy of model polymer nanocomposites. Nanotechnology 2011;22:175706.
[21] Sahin O, Quate CF, Solgaard O, Atalar A. An atomic force microscope tip designed to measure time-varying nanomechanical forces. Nat Nanotechnol 2007;2:507.
[22] Jesse S, Kalinin SV, Proksch R, Baddorf AP, Rodriguez BJ. Energy dissipation measurements on the nanoscale: band excitation method in scanning probe microscopy. Nanotechnology 2007;18:435503.
[23] Rico F, Su C, Scheuring S. Mechanical mapping of single membrane proteins at submolecular resolution. Nano Lett 2011;11:3983–6.
[24] Platz D, Tholén EA, Haviland DB. Intermodulation atomic force microscopy. Appl Phys Lett 2008;92:153106.
[25] Proksch R. Multifrequency, repulsive-mode amplitude-modulated atomic force microscopy. Appl Phys Lett 2006;89:113121.
[26] Martinez NF, Patil S, Lozano JR, Garcia R. Enhanced compositional sensitivity in atomic force microscopy by the excitation of the first two flexural modes. Appl Phys Lett 2006;89:153115.
[27] Garcia R. Amplitude modulation AFM. Weinheim (Germany): Wiley-VCH; 2010.
[28] Raman A, Melcher J, Tung R. Cantilever dynamics in atomic force microscopy. Nano Today 2008;3:20.
[29] Stark RW. Bistability, higher harmonics, and chaos in AFM. Mater Today 2010;13:24–32.
[30] Patil S, Martinez NF, Lozano JR, Garcia R. Force microscopy imaging of individual protein molecules with sub-pico Newton force sensitivity. J Mol Recognit 2007;20:516.
[31] Martinez NF, Lozano JR, Herruzo ET, Garcia F, Ritchter C, Sulzbach T, et al. Bimodal atomic force microscopy imaging of isolated antibodies in air and liquids. Nanotechnology 2008;19:384011.
[32] Stark RW. Dynamics of repulsive dual-frequency atomic force microscopy. Appl Phys Lett 2009;94:063109.
[33] Dick AJ, Solares SD. Utilizing off-resonance and dual-frequency excitation to distinguish attractive and repulsive surface forces in atomic force microscopy. J Comp Nonlinear Dyn 2011;6:031005.
[34] Chawla G, Solares SD. Mapping of conservative and dissipative interactions in bimodal atomic force microscopy using open-loop and phase-locked control of the higher eigenmode. Appl Phys Lett 2011;99:074103.
[35] Dietz C, Zerson M, Riesch C, Gigler AM, Stark RW, Rehse N, et al. Nanotomography with enhanced resolution using bimodal AFM. Appl Phys Lett 2008;92:143107.
[36] Gigler A et al. Repulsive bimodal atomic force microscopy on polymers. Beilstein J Nanotechnol 2012;3:456–63.
[37] Albonetti C, Casalini S, Borgatti F, Floreano F, Biscarini F. Morphological and mechanical properties of alkanethiol self-assembled monolayers investigated via bimodal AFM. Chem Commun 2011;47:8823–5.
[38] Aksoy MD, Atalar A. Force spectroscopy using bimodal frequency modulation atomic force microscopy. Phys Rev B 2011;83:075416.
[39] Li JW, Cleveland JP, Proksch R. Bimodal magnetic force microscopy: Separation of short and long range forces. Appl Phys Lett 2009;94:163118.
[40] Dietz C, Herruzo ET, Lozano JR, Garcia R. Nanomechanical coupling enables detection and imaging of 5 nm superparamagnetic particles in liquid. Nanotechnology 2011;22:125708.
[41] Stark RW, Naujoks N, Stemmer A. Multifrequency electrostatic force microscopy in the repulsive regime. Nanotechnology 2007;18:065502.
[42] Bostanci U, Abak MK, Aktas O, Dâna A. Nanoscale charging hysteresis measurements by multifrequency electrostatic force spectroscopy. Appl Phys Lett 2008;92:093108.
[43] Ding XD et al. Improving lateral resolution of electrostatic force microscopy by multifrequency method under ambient conditions. Appl Phys Lett 2009;94:223109.
[44] Kawai S et al. Measuring electric field induced subpicometer displacement of step edge ions. Phys Rev Lett 2012;109:146101.

[45] Garcia R, Perez R. Dynamic atomic force microscopy methods. Surf Sci Rep 2002;47:197.
[46] Kawai S, Glatzel T, Koch S, Such B, Baratoff A, Meyer E. Systematic achievement of improved atomic-scale contrast via bimodal dynamic force microscopy. Phys Rev Lett 2009;103:220801.
[47] Naitoh Y, Ma Z, Li Y, Kageshima J, Sugawara M, Vac YJ. Sci Technol B 2010;28:1210.
[48] Kawai S, Glatzel T, Koch S, Such B, Baratoff A, Meyer E. Ultrasensitive detection of lateral atomic-scale interactions on graphite (0001) via bimodal dynamic force measurements. Phys Rev B 2010;81:085420.
[49] Solares SD, Chawla G. Frequency response of higher cantilever eigenmodes in bimodal and trimodal tapping mode atomic force microscopy. Meas Sci Technol 2010;21:125502.
[50] Solares SD, Chawla G. Triple-frequency intermittent contact atomic force microscopy characterization: simultaneous topographical, phase, and frequency shift contrast in ambient air. J Appl Phys 2010;108:054901.
[51] Lozano JR, Garcia R. Theory of multifrequency AFM. Phys Rev Lett 2008;100:076102.
[52] Lozano JR, Garcia R. Theory of phase spectroscopy in bimodal AFM. Phys Rev B 2009;79:014110.
[53] Herruzo ET, Garcia R. Theoretical study of the frequency shift in bimodal FM–AFM by fractional calculus. Beilstein J Nanotechnol 2012;3:198–206.
[54] Sader JJE, Uchihashi T, Higgins MJ, Farrell A, Nakayama Y, Jarvis SP. Quantitative force measurments using frequency modulation atomic force microscopy – theoretical foundations. Nanotechnology 2005;16:S94–S101.
[55] San Paulo A, Garcia R. Tip-surface forces, amplitude, and energy dissipation in amplitude modulation (tapping-mode) force microscopy. Phys Rev B 2001;64:193411.
[56] Martinez-Martin D, Herruzo ET, Dietz C, Gomez-Herrero J, Garcia R. Noninvasive protein structural flexibility mapping by bimodal dynamic force microscopy. Phys Rev Lett 2011;106:198101.
[57] Giessibl FJ. Forces and frequency shifts in atomic-resolution dynamic-force microscopy. Phys Rev B 1997;56:16010–5.
[58] Proksch R, Yablon DG. Loss tangent imaging: theory and simulations of repulsive-mode tapping atomic force microscopy. Appl Phys Lett 2012;100:073106.
[59] US National Institute of Standards and Technology (NIST) Ultra High Molecular Weight Polyethelene, Ref Mater 8456.
[60] Walters DA, Cleveland JP, Thomson NH, Hansma PK, et al. Short cantilevers for atomic force microscopy. Rev Sci Inst 1996;67:3583–90.
[61] For example, the BW is about 10 MHz for the Cypher AFM, then $f_{0,2} \leqslant 10$MHz (Asylum Instruments Corporation, USA).
[62] Zaccai G. How soft is a protein ? A protein dynamics force constant measured by neutron scattering. Science 2000;288:1604–7.
[63] Dong M, Husale S, Sahin O. Determination of protein structural flexibility by microsecond force spectroscopy. Nat Nanotechnol 2009;4:514.
[64] Schwarz A, Wiesendanger R. Magnetic sensitive force microscopy. Nano Today 2008;3:28–39.
[65] Herruzo ET, Asakawa H, Fukuma T, Garcia R. Three-dimensional quantitative force maps in liquid with 10 piconewton, angstrom and sub-minute resolutions. Nanoscale 2013;5:2678–85.
[66] Wang J, Boisvert DC. Structural basis for GroEL-assisted protein folding from the crystal structure of (GroEL-KMgATP)(14) at 2.0 angstrom resolution. J Mol Biol 2003;327:843–55.
[67] Yamada H, Kobayashi K, Fukuma T, Hirata Y, Kajita T, Matsushige K. Molecular resolution imaging of protein molecules in liquid using frequency modulation atomic force microscopy. Appl Phys Express 2009;2(095):007.

**Ricardo Garcia** has designed a number of scanning probe microscopy techniques. He has also contributed to the development of tip-based nanolithography. He has published in a wide range of journals such as Science, Nature Nanotechnology or Cell. RG is co-author of 115 publications (over 5500 citations and an *h-index* of 39), and one book on dynamic force microscopy. RG holds a portfolio of 10 patents, four of them have been licensed for commercial exploitation. RG has been elected fellow of the American Physical Society in 2007 and promoted to Full Professor at CSIC in 2004.

**Roger Proksch** is President and co-founder of Asylum Research. He has over 25 years of experience in the development of force microscopes. He has over 80 scientific papers and is an inventor on over 30 patents granted and pending. Previously, he was the Director of Magnetics Research at Digital Instruments and a Professor at St. Olaf College. He received his PhD from the University of Minnesota and was a post-doc at UC-Santa Barbara.